Available online at www.sciencedirect.com

ScienceDirect

journal homepage: www.elsevier.com/locate/he

High selectivity to hydrogen on the methane decomposition over Rh/γ-Al_2O_3–Nd_2O_3 catalysts

M. Caballero [a], G. Del Angel [a,*], A. Bonilla-Sánchez [a], I. Rangel-Vázquez [a], A. Arrieta [a], A. Vázquez-Zavala [a], L. Huerta [b,1], M. Salgado [a]

[a] Universidad Autónoma Metropolitana-Unidad Iztapalapa, Departamento de Química, Área de Catálisis, Av. San Rafael Atlixco No. 186, C.P. 09340, A.P 55-534, México D. F., Mexico

[b] Instituto de Investigaciones en Materiales, Universidad Nacional Autónoma de México, Apartado Postal 70-360, México D.F., 04510, Mexico

ARTICLE INFO

Article history:
Received 1 June 2016
Received in revised form
1 October 2016
Accepted 2 October 2016
Available online 7 November 2016

Keywords:
Hydrogen
Methane
Rhodium
Neodymium
Carbon
SEM-EDS

ABSTRACT

Methane decomposition was carried out on Rh/γ-Al_2O_3 and Rh/γ-Al_2O_3–Nd_2O_3 catalysts to produce hydrogen. γ-Al_2O_3–Nd_2O_3 mixed oxides and Rh/γ-Al_2O_3–Nd_2O_3 catalysts were prepared by wet impregnation using $Nd(NO_3)_3 \cdot 6H_2O$ and $RhCl_3 \cdot 3H_2O$ as precursors. The concentrations for the catalysts were 1.0 wt% for Rh and 1 and 10 wt% for Nd. The reaction was carried out from 400 to 750 °C. All catalysts showed high activity and selectivity at 700 °C, with conversions around 74–79 vol%. The activity per site (TOF) was higher on Rh crystallites size ≥2.1 nm. The Rh catalyst with 10 wt% neodymium concentration was highly selective to hydrogen, 100%. This behavior was explained by the highest interaction between Rh and γ-Al_2O_3–Nd_2O_3 supports. Rh/γ-Al_2O_3 and Rh/γ-Al_2O_3–Nd_2O_3 with 1 wt% Nd showed selectivities of 89 and 65% at 700 °C respectively and ethane and ethylene products. These products come from the mobility of CHx species on the Rh surface during the reaction. The carbon produced was mainly deposited on the support. Characterization was done by XRD, N_2 adsorption isotherms, HRTEM, EDS-SEM, CO-FTIR, H_2-TPR, XPS.

Introduction

Nowadays there is a clear need to find an alternative energy source that will replace, at least partially and progressively, fossil fuels in the near future and hydrogen seems to be one of the most promising energy sources, since it is considered as environmentally benign [1]. The amount of energy produced during the hydrogen combustion is higher than that obtained by any other fuel. The advantages of hydrogen as an energy source is that it represents an abundant raw material and its combustion does not produce CO_2, but only water vapor, which makes it an ideal candidate for the reduction of the so-called "greenhouse effect" [2–4].

Nowadays, the main process for producing hydrogen is steam reforming of natural gas [5]. Steam reforming is a multiple stage process. The first stage is conducted at high temperature (800–900 °C). While the second stage is the catalytic water gas shift reaction, occurring in two steps. In addition to steam reforming, partial oxidation is also used to generate hydrogen from fossil fuels [6], but the produced hydrogen is still mixed with CO and CO_2, which again needs a

* Corresponding author.
E-mail address: gdam@xanum.uam.mx (G. Del Angel).
[1] Fax: +52 55 5622 4715.

http://dx.doi.org/10.1016/j.ijhydene.2016.10.001

complicated separation process as in the steam reforming case.

The energy required for methane catalytic cracking is nearly one half that required for steam reforming per mole of methane decomposed [7–9]. The energy requirement is 37.4 kJ/mol H_2 in methane catalytic cracking compared to 63.3 kJ/mol H_2 in the steam reforming process [9]. In addition to the lower energy demand for methane catalytic cracking compared to steam reforming, there is no need for additional energy for steam generation or gas treatment. The heat requirement for catalytic cracking can be covered by burning ~15–20% of the hydrogen produced, which further reduces CO_2 emissions [10].

Contrasting the steam reforming process, the catalytic decomposition of methane does not include water gas shift and preferential oxidation of CO, which considerably simplifies the process and may reduce the hydrogen production costs [11].

Steinberg and Cheng [12] compared different methods for hydrogen production at an industrial scale of 10^8 SCF/D (Standard Cubic Feet per Day) of hydrogen gas at 300–600 psig. They concluded that methane thermal cracking is the most economical method for hydrogen production followed by Hydrocarbon process ‹ steam reforming ‹ Coal gasification with electricity chemical shift (Westinghouse) ‹ Partial oxidation ‹ Steam iron ‹ High temperature steam electrolysis ‹ Texaco gasification ‹ Coal gasification with high temperature electrolysis ‹ K-T gasification ‹ Water electrolysis.

Recent investigations have focused on improving the process of hydrogen production by decomposition of methane to form hydrogen and elemental carbon as an attractive alternative to the steam reforming [10], using metal or carbon catalysts for a higher conversion of methane and stability long-term catalyst [13–15]. In recent years different metal based catalysts mono and bimetallic have been studied in the hydrogen production as Fe [16], Ni–Cu–Fe/Al_2O_3 [17].

For simultaneous production of hydrogen and nanocarbon particles, nickel-based catalysts have been used. However, the major drawback in the case of the decomposition on metal catalysts (Ni, Co or Fe), is that the catalyst is quickly deactivated because of deposits of carbon [18,19]. In general, the noble metals show better catalytic activity and resistance to the deactivation, but the use of the catalysts based Ni is due to its lower cost [20].

In recent years, the investigation of the behavior of the addition of lanthanides elements to noble metal catalyst has begun [21,22]. Manoj et al. [23] concluded that yield of hydrogen and carbon increased significantly with increasing the reaction temperature from 600 °C to 700 °C. A maximum initial hydrogen yield of 62%, 61% and 58% and a final carbon yield of 1360 wt%, 1159 wt% and 1576 wt% was achieved over ceria, zirconia and lanthana supported catalysts respectively, at 700 °C.

Ahmed et al. [24] studied Catalytic methane decomposition in a fixed bed reactor. The effect of promoting Fe with Ce and Co and reduction temperature is investigated. The results reveal that Ce addition has shown a negative impact on H_2 yield while a positive effect on H_2 yield and catalyst stability are observed with Co addition. In terms of number of moles of hydrogen produced per active sites, Fe/Al_2O_3 has shown a higher number of moles of hydrogen compared to bimetallic catalysts.

Tang et al. [25] employed Fe/CeO_2 for methane decomposition using a fixed bed reactor at 750 °C. The optimum activity was observed with a catalyst composed of 60 wt. % Fe_2O_3 and 40 wt. % CeO_2. CO was detected due to carbon oxidation by high mobility lattice oxygen from Ceria. Comparing Fe and Ceria and Fe–Ce bimetallic catalysts, Ce monometallic catalyst showed very small CH_4 conversion activity. Fe catalyst showed 60% CH_4 conversion after 25 min, then the catalyst was completely deactivated after 50 min.

As example it has been assumed that the component of cerium has a crucial role in the maintenance of the catalytic activity of noble metals, at the same time, the oxide of cerium shows a good stability in presence of precious metals, such as Ru, Rh, Pd, Pt, and can lead to decrease the carbon deposit during the decomposition of methane. The purpose of the present study was to investigate the influence of rare-earth as Neodymium on the Rh/γAl_2O_3–Nd_2O_3 catalysts in the activity, selectivity and stability of Rh for the CH_4 decomposition. Two concentrations of Nd (1 and 10 wt%) in the Rh catalysts where evaluated in the decomposition of CH_4 to produce hydrogen. The γ-Al_2O_3 was selected because of its high specific surface area and also it has reported good activity on Rh supported on alumina for CH_4 reforming. Neodymium was selected to give stability to the alumina and because it is not widely used in this type of reaction.

The characterization was done by N_2 adsorption-desorption, X-ray diffraction, H_2-TPR, FTIR of CO adsorption, XPS, HRTEM, SEM-EDS.

Experimental

Supports and catalysts preparation

γ-Al_2O_3 support was prepared from Bohemita Catapal B. Firstly the Boehmite was dried to 120 °C for 12 h, then the solid was calcined in air flow of 60 mL/min for 24 h using a ramp of temperature from 25 °C to 650 °C. The γ-Al_2O_3–Nd_2O_3 (loaded with 1 and 10 wt% Nd) mixed oxides, were prepared by wet impregnation of the Boehmite with the necessary quantity of $Nd(NO_3)_3 \cdot 6H_2O$ (Strem Chemicals, 99.99%) aqueous solutions to obtain 1 and 10 wt% of Nd on the support, the mixture was maintained in stirring for 3 h. Then, the solids were dried in an oven to 120 °C for 12 h, after that, samples were calcined at 650 °C in airflow of 60 mL/min for 24 h.

Rh catalysts were prepared by wet impregnation of the γ-Al_2O_3–Nd_2O_3 supports with $RhCl_3 \cdot 3H_2O$ (Strem Chemicals, 99.99%) aqueous solution. The solids were left in stirring for 3 h, and then, the water is evaporated using a vacuum evaporator bath at 60 °C and vacuum of 72 millibars. Subsequently the solids were dried in an oven at 120 °C, for 12 h. The catalysts were calcined in air at 500 °C under airflow of 60 mL/min for 5 h and finally reduced in H_2 flow of 60 mL/min at 500 °C for 5 h. The Rh percentage on the catalysts was obtained by atomic absorption technique. Catalysts were labeled as: RhANdX, where: Rhodium, as Rh, alumina as A, neodymium as Nd, and X is the concentration of Neodymium in wt%.

Catalysts characterization

The BET surface area of the catalysts was measured using a Quantachrome Multistation Autosorb 3B analyzer. Nitrogen was used as the measuring gas at −196 °C. Before adsorption, the sample (100 mg) was outgassed at 300 °C under vacuum (10^{-3} Torr) for 24 h in order to eliminate moisture and impurities physically adsorbed on the surface of the solid. The specific surface areas were calculated with the BET equation and the mean pore size by the BJH method.

The X-ray diffraction patterns of the supports were obtained using a Bruker D-8 Advance X-ray powder diffractometer equipped with a Cu Kα radiation anode in Bragg-Brentano geometry. The detection was carried out using a Lynxeye detector, which is a linear-type. Intensity data was measured in continuous mode through the 2θ ranges between 10° and 70° with a 2θ step of 0.02°.

The TPR determinations were carried out in a Chembet-3000 (Quantachrome Co) apparatus using 0.2 g of catalyst by means of the following protocol: samples were heated at 300 °C under nitrogen flow (10 mL min^{-1}) for 30 min. Then, the samples were cooled dawn to room temperature and a mixed gas flow (5%H_2/95%N_2) was passed through the cell. The TPR profiles were recorded by heating the sample from room temperature up to 600 °C at a rate of 10 °C/min under the gas mixture of 10 mL min^{-1}.

XPS analysis was performed on a Kratos photoelectron spectrometer computer with axis ULTRA of X-ray with an analyzer of hemispherical electron energy of 165 mm. The incident radiation is produced from the monochromatic Al X -rays (1486.6 eV) at 225 W (15 kV, 15 mA). The study (extended) was taken with an analyzer at a pass energy of 160 eV and multiplex (narrow) with high-res scans with pass energy of 20 eV. Scanning was performed with binding energy range 1200–0 eV in steps of 1.0 eV and dwell time of 100 ms. High resolution scans were performed with 0.05 eV and 250 ms dwell time. The base pressure in the analysis chamber was 1.0×10^{-9} Torr during the analysis of the sample was 1.0×10^{-8} Torr. XPS spectra were fitted with the program SDP v 4.1 [26].

Transmission electron microscopy (TEM) study was performed on an electron microscope of field emission that operates at 200 kV. The microscope is equipped with a field of Schottky type emission cannon and a configuration of ultra-high resolution (UHR) (Cs = 0.5 mm; Cc 1.1 mm; point to point resolution, 0.19 nm). The samples were also characterized by high angle annular dark field detector (HAADF) used when the microscope became operate in STEM mode known as "Z contrast". The samples were powdered in an agate mortar and were suspended in ethanol at room temperature and dispersed in an ultrasonic bath for two minutes, then one drop of the solution was deposited on a carbon copper grid. It is important to note that the samples were transported in a plastic bag filled with argon in order to prevent the contamination of O_2.

EDS analysis was performed in a fiel emission microscope HRSEM Jeol 7600F with a detector Oxford instruments X-MAX 20 mm^2 (SDD), detector allows high-resolution mapping. Equipment with an acceleration voltage of 15 kV. Quantification is statistic result of quantifications 9 spectra in nine areas of the sample, the mean values wt% and standard deviations obtained.

HRTEM-FFT. The high Resolution Transmission Electron Microscopy was measured in a HRTEM-2010F JEOL equipped with a field emission source and an acceleration of 200 kV. The sample was grinded and dispersed on a holey carbon film grid of 300 meshes, and the high-resolution images were obtained from the transmission of electrons that go through the floating sample. The measure of the crystallographic planes was done by using a Digital Micrograph program by the Gatan software team.

FT-IR of CO adsorption spectra was determined at room temperature by using a FTIR Nicolet 170-SX apparatus, with a resolution of 2 cm^{-1}. The sample pressed in thin wafers were placed in a Pyrex glass cell, equipped with CaF_2 windows, coupled to a vacuum system and gas lines supplied. The samples were maintained under vacuum (10^{-3} Torr) at 400 °C for 30 min. Then, the cell was cooled to room temperature and the CO (Praxair UHP) admission of 20 Torr was carried out. The CO excess was evacuated during 30 min, after the CO adsorbed FTIR spectra were recorded.

Catalytic tests

The activity determinations were carried out in a quartz glass micro-reactor system with a fixed bed at atmospheric pressure and catalyst load of 0.05 g. The reaction temperatures varied from 400 to 700 °C, the increase of temperature was on steps of 100 °C and the last at 750 °C with a rate of 5 °C min^{-1}. Experiments consisted in a previous thermal treatment to the catalysts with flowing nitrogen for 15 min at 300 °C. Then, a pure CH_4 (99.999%) feed steam (2 mL min^{-1}) was introduced into the reactor. The inlet and outlet effluents were monitored on line gas chromatograph, Shimadzu GC-2014 equipped with 6 packed columns and TCD and FID detectors. Which allows the measurement of inorganic gases (H_2, CO and CO_2) and organic hydrocarbons as CH_4, C_2H_4, and C_2H_6. The identification reaction products were accomplished by the quantification of them, which were carried out with calibration curves of products reaction using the appropriate software. The methane conversion was calculated as the amount of methane converted throughout the experiment over the amount admitted during that step. The selectivity was the amount of each product H_2, C_2H_4, or C_2H_6 collected at reactor outlet over the methane converted.

Results and discusion

Catalysts characterization

The diffraction patterns of the Rh catalysts supported on γ-Al_2O_3 and γ-Al_2O_3–Nd_2O_3, which were normalized, are showed in Fig. 1. The RhA catalysts show the characteristic peaks of gamma alumina phase (JCPDS PDF 056-0457 Quality: Rietveld). The diffraction pattern of RhANd1 catalyst supported on γ-Al_2O_3 containing 1 wt% Nd (JCPDS PDF 01-079-9858 Quality: Star (*)) does not show notable difference in

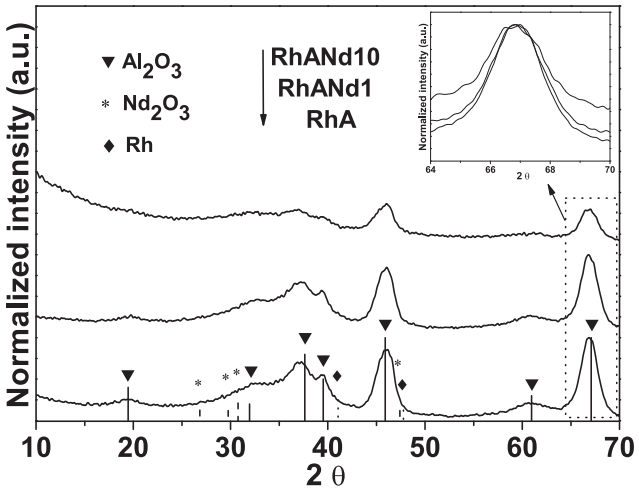

Fig. 1 – X-ray diffractions patterns for RhA and RhANd1 and RhANd10 catalysts.

respect to the diffractogram for RhA catalyst. However, the presence of 10 wt% Nd in RhANd10 catalyst leads to a modification of the diffraction pattern. Lower intensity of alumina peaks is observed, which indicate low crystallinity of the solid. The presence of neodymium at 10 wt% inhibited the growth of the alumina crystals [27]. In Fig. 1 is plotted an inset where is observed the peaks of the alumina having maxima at around 67° in 2θ. The increase in the broad peak is related with the reduction of the crystallite size as the concentration of Nd_2O_3 increases. There were not detected peaks for Nd (1 and 10 wt %) neither for Rh (JCPDS PDF 05-0685 Quality: Star (*) (0.7–0.86 wt%), due probably to the low concentration, which could not be detected by the equipment or due to the high dispersion on the alumina surface. On the other hand the likely replacement of Al^{3+} ions by the Nd^{3+} ions inside of the alumina structure seams not to be totally produced since Nd^{3+} presents ionic radii of 1.08 Å with a hexagonal structure, while Al^{3+} has a fcc crystalline structure and an ionic radii of 0.5 Å. The ionic radii of neodymium are larger than the Al^{3+}, which difficult the atomic substitution in the alumina structure network. But a probably small integration cause a perturbation in the crystal structure of the alumina hindering the growth of the crystallites [27]. At the highest Nd content a probable segregation of this element can be found on the alumina surface as neodymium oxide, then a Nd_2O_3 enriched surface on the RhANd10 catalyst is expected [28].

The BET specific surface areas of the catalysts is reported in Table 1. The BET surface area for alumina (A) support is 266 $m^2\ g^{-1}$, and for RhA catalyst, 284 $m^2\ g^{-1}$. The catalysts containing neodymium RhANd1 and RhANd10 show a slight decrease of the surface area (237 and 227 $m^2\ g^{-1}$) in respect to that observed in the A support and RhA catalyst references. The most affected catalysts was RhANd10 which shows a decrease around 20%. This result can be explained by an occlure of the pore, which increases with the amount of promoter, Table 1. In Fig. 2 is depicted the pore size distribution of the rhodium catalysts, where is showed a similar pore size distribution on RhA and RhANd1, with values of mean pore size of 48 and 49 Å respectively. The RhANd10 catalyst presented a pore size distribution profile shifted towards lower values giving a lower mean pore size, 39 Å. The pore volume presents a decrease tendency with the increasing amount of Nd in the catalyst. This behavior would be due to deposition of Nd_2O_3 at th alumina pores mouth, producing an apparent small pore but with the expected decrease in surface area.

The concentrations of Rh on the catalysts were determined by atomic absorption and reported in Table 1. The nominal concentration of Rh was 1.0wt%, the real concentrations are 0.77, 0.70 and 0.86 wt%, and these values can be considered valid, in the error range.

The mean Rh crystallite size of the fresh catalysts determined by TEM is reported in Table 1. The micrograph and the

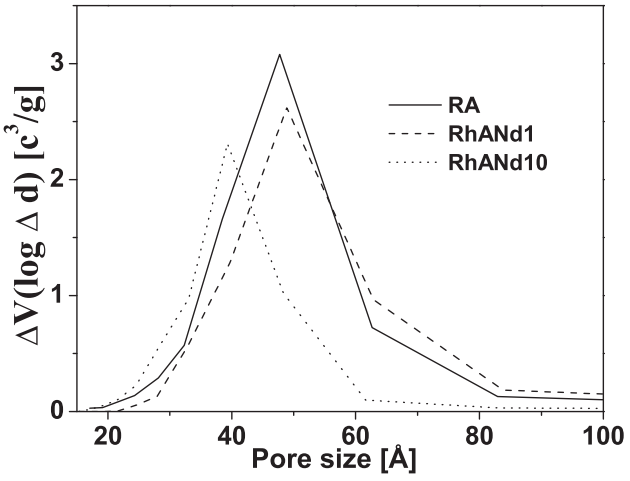

Fig. 2 – Pore Size diameter distribution for Rh catalysts.

Table 1 – Characteristics of the Rh catalysts.

Catalysts[a]	Rh (wt%)[b]	Mean size Rh crystallite (nm)	% D[c]	Pore volume cc g^{-1}	Pore size Å	Area BET $m^2\ g^{-1}$
RhA	0.77	1.0 ± 0.30	100	0.638	48	(266) 284[d]
RhANd1	0.70	2.1 ± 0.48	52	0.575	49	237
RhANd10	0.86	3.3 ± 0.72	33	0.439	39	227

[a] Fresh catalysts.
[b] Atomic Absorption Technique.
[c] Dispersion (%) = ($^aN_{(S)}$ Rh/$^bN_{(T)}$ Rh) × 100. $^aN_{(S)}$ Rh = Number of active Rhodium atoms available for reaction. $^bN_{(T)}$ Rh = Total number of Rhodium atoms in the catalyst material.
[d] Specific surface area for alumina (A) support.

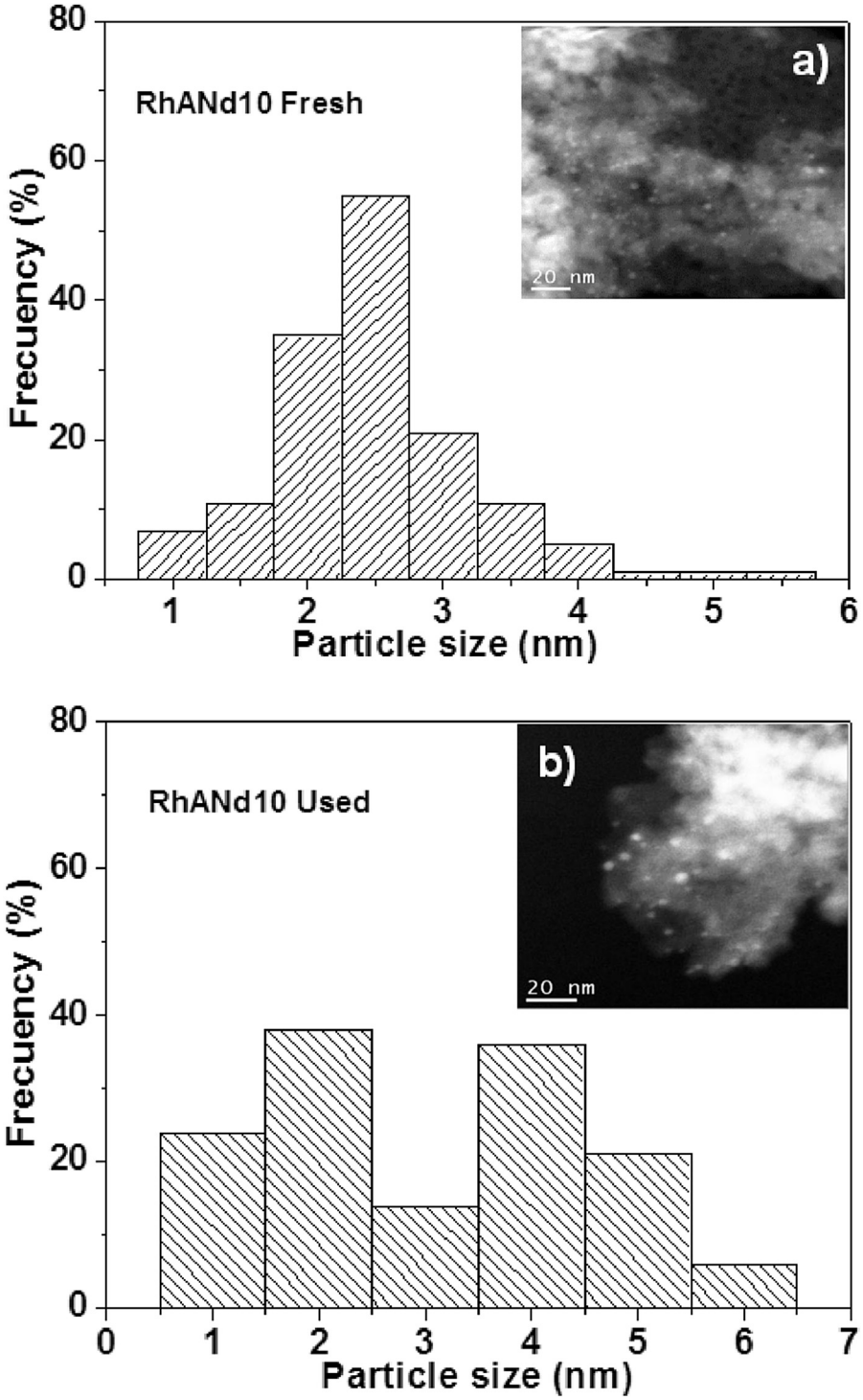

Fig. 3 – TEM images and histograms of metal crystallite size distribution for the RhANd10 and RhANd10-used catalysts.

distribution of the Rh crystallite size for a selected RhANd10 fresh catalyst is depicted in Fig. 3a). The mean Rh crystallite size for all catalysts were determined by $ds = \Sigma n_i d_i^3 / n_i d_i^2$ equation, where ds, is the mean crystallite size of Rh, n_i, the number of Rh crystallite diameter d_i, measured directly on the micrographs, at least 150 Rh particles were counted. The histogram analysis clearly suggests a narrow size distribution (Fig. 3). The mean Rh crystallite size was 1.0, 2.1 and 3.3 nm for RhA, RhANd1 and RhANd10 for the fresh catalysts respectively, Table 1. The dispersion of Rh catalysts is also reported in the Table 1, calculated by D(%) = Number of active Rh atoms available for reaction/Total number of Rh atoms in the catalyst material $\times 100$.

The reduction profiles (H_2-TPR) for RhA, RhANd1 and RhANd10 catalysts are shown in Fig. 4. Two reduction peaks were observed in all Rh samples. RhA and RhANd1 catalysts

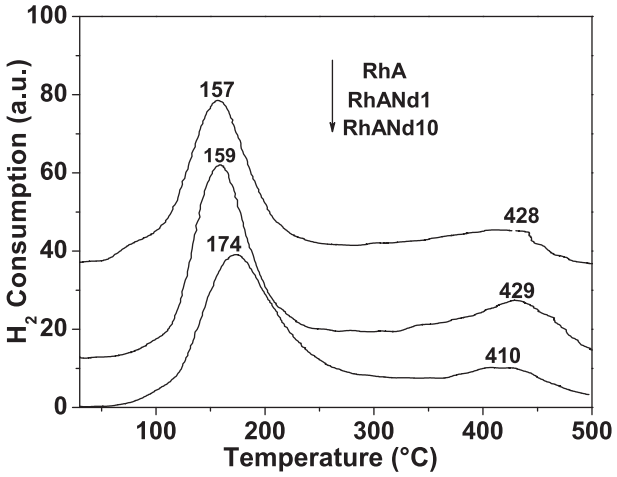

Fig. 4 – H_2-TPR profiles of neodymium promoted RhA and RhANd1 and RhANd10 catalysts.

exhibited a similar lower reduction temperature peak at 157 and 159 °C respectively, which has been attributed to the reduction of three dimensional Rh_2O_3 crystallites on alumina Rh supported catalyst to give metallic rhodium [28,29]. This rhodium oxide specie is closely interacting with the alumina surface [30,31]. The Rh catalyst with 1 wt% Nd as promoter (RhANd1) practically does not modify the reduction temperature of Rh_2O_3 specie, indicating similar interaction of Rh with the surface as in the RhA catalyst.

For RhANd10 catalyst the first peak is shifted towards higher temperature, the reduction peak is centered at 174 °C, corresponding to the reduction of three dimensional Rh_2O_3 particles to get metallic Rh [32]. Burch et al. proposed that when Rh is calcined at 500 °C some Rh oxide may spread on the support and placed on the alumina defects sites and Rh become strongly bounded and hardly-reducible [28]. Some authors have reported that Rh_2O_3 and Nd_2O_3 compounds show a great affinity in an oxidizing atmosphere resulting Rh interacting strongly with Nd_2O_3 and the Rh–O–Nd bond formation [33]. The shift of Rh reduction to higher temperature could be originated from a higher interaction between the Rh and the neodymium oxide in the oxidizing atmosphere of calcinations pretreatments [28]. In the present case a strong interaction of the Rh with the Nd_2O_3 on the surface and a probable formation of Rh–O–Nd bond on the surface could occur. Then, Rh support interaction with a Nd_2O_3-enriched surface layer in RhNd10 sample is the responsible of the temperature shift of Rh reduction peak because this sample has the highest amount of Nd_2O_3 (10 wt%) and whose excess would be highly deposited on the alumina surface with large interaction with Rh particles.

The second reduction peak at the highest temperature show a maximum at 428 °C, 429 °C and 410 °C for RhA, RhANd1 and RhANd10 catalysts, this peak has been associated to reduction of a rhodium oxidized specie, $Rh(AlO_3)$, formed by diffusion of Rh oxides into sub layers of γ-Al_2O_3 structure at high temperatures [30]. Although, other authors have proposed that this second peak is related to the reduction of two dimensional Rh_2O_3 particles [30].

Table 2 – Binding energy of Rh $3d_{5/2}$ core level and relative abundance of the different species of Rh from XPS data in RhA and RhANdX catalysts.

Catalyst	Binding energy (eV)		Abundance (%)	
	Rh°	Rh^{3+}	Rh°	Rh^{3+}
RhA	307.25	308.45	42	58
RhANd1	307.25	308.45	33	67
RhANd10	307.25	308.45	25	75

The above results are in good agreement with those obtained by X-ray photoelectron spectroscopy (XPS). The X-ray photoelectron data of Rh 3d region for Rh catalysts are reported in Table 2 and the XPS spectra are shown in Fig. 5. The binding energies (BE) of Rh corresponding to the Rh $3d_{5/2}$ core level show 2 peaks at 307.25 eV and 308.45 eV which can be ascribed to Rh° and Rh^{3+} species for all the Rh catalysts, bare RhA, RhANd1 and RhANd10 catalysts. The relative abundance of the reduced and oxidized specie was calculated from the area of the deconvoluted peaks. For RhA, RhANd1 and RhANd10 (Table 2) the relative amount of Rh° specie varies from 42, 33 and 25% whereas for Rh^{3+} species the amounts are 58, 67 and 75% respectively. An increase of the oxidized specie with the increase of the Nd_2O_3 in the catalyst is observed, the presence of Nd_2O_3 stabilize the Rh^{3+} oxidized specie. These results suggest that the presence of Nd_2O_3 in Rh catalysts yield Rh electro-deficient species as a result of the strong interaction of Rh with the Nd_2O-enriched surface layer on the RhANd10 catalyst. XPS results confirm the suggestions proposed above of a stronger interaction metal-support on the catalyst with the highest content of Nd_2O_3.

The FTIR of CO adsorbed on the Rh catalysts promoted and unpromoted is showed in Fig. 6. RhA catalyst shows a similar spectra to the ones reported by other authors [34]. The two only peaks are depicted at 2091 and 2019 cm^{-1} which are associated to symmetrical and asymmetrical stretching vibration of germinal-dicarbonyl $Rh^{+}(CO)_2$ species. The presence of this species is explained by the oxidative disruption of Rh crystallites comprising hydroxyl groups of the support [35,36]. Neither the bridged-bonded CO species (1850 cm^{-1}) nor the CO linearly bonded species on Rh° (2040–2070 cm^{-1}) were detected, species formed on large Rh surface [35]. The presence of gem-dicarbonyl species in the FTIR spectrum for RhA catalyst should be interpreted as the presence of very small rhodium crystallites corresponding to high dispersion. Then, it can be assumed that CO gem-dicarbonyl form adsorbs in low coordinated sites. In the same way for the RhANd1 and RhANd10 catalysts the dicarbonyl species bands were the unique CO absorption bands detected. However, the trend observed in these samples is that with the increase of Nd loading a diminution of the IR intensity of the CO bands is produced. This behavior was more notable in the sample with higher amount of Nd (10 wt%). The diminution of the intensity with the addition of Nd promotor could be related to the difference of Rh crystallite size. If the Rh crystallite size increases it should be noticed the presence of the linear CO adsorption band, however this is not the case here. A crystallite size larger than the ones obtained in our catalysts is required for the

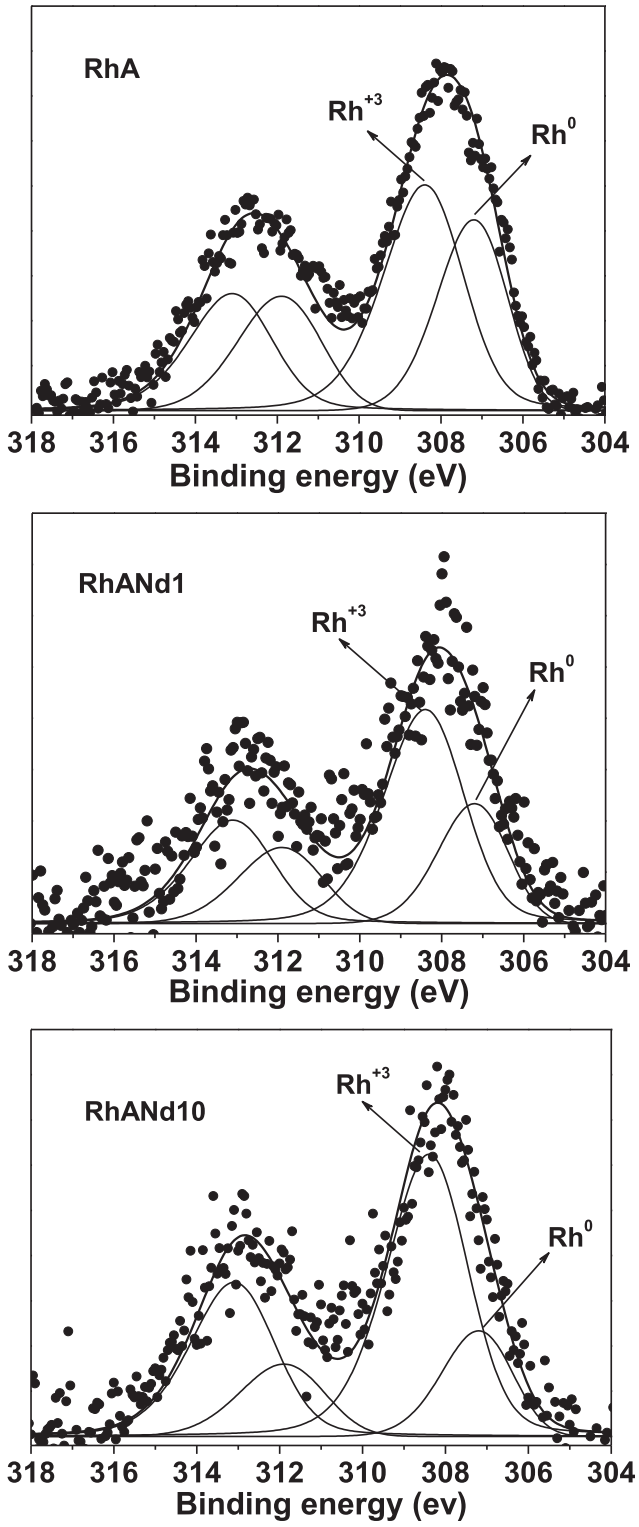

Fig. 5 – XPS spectra of Rh 3d core level for RhA and RhANd1 and RhANd10 catalysts.

obtention of the CO linear adsorption on rhodium metal. On the other hand, it is probable that the reduction in intensity of IR bands is due to a diminution of the number of Rh sites of low coordination exposed to CO adsorption by progressive blockage by the neodymium oxide [29].

Activity, selectivity and carbon

Methane dehydrogenation was conducted at temperatures of 400, 500, 600, 700 and 750 °C with undiluted methane flow and a space velocity of 6 L h^{-1} g^{-1}. Fig. 7 shows the profiles of methane conversion as function of temperature. It can be seen that the conversion of methane increases as the temperature increases from 400 °C to a maximum conversion at 700 °C, then a diminution is observed at 750 °C.

The methane dehydrogenation for the different catalysts at 400 °C shows good activity showing conversions of 50, 45 and 39 vol%, corresponding to RhANd1, the most active, followed of RhA and RhANd10, respectively (Table 3). Moreover, the activity per site, TOF h^{-1} (turn-over frequency) for the decomposition of methane, the RhANd1 and RhANd10 catalyst showed the highest activity (14 h^{-1}) followed by RhA (5.5 h^{-1}) catalysts, Table 3. As it is also well known the structure of the metal particle can influence in the activity [37]. The RA sample with the lowest crystallite size (1.0 nm) shows also the lowest activity per site. At particles size ≥2.0 nm the activity is higher, larger Rh crystallite size are more active at 400 °C (Table 3).

All Rh catalysts exhibit the highest performance at 700 °C (Fig. 7). The conversion of the reaction increased rapidly between 600 and 700 °C, this can be explained by the reduction of more active Rh sites using, in situ, hydrogen produced at 700 °C [38,39]. The maximum conversion of methane dehydrogenation is around of 74–79 vol% at 700 °C for all Rh catalysts (Table 4). Nevertheless, the activity per active site (TOF) is higher with the presence of Nd in the catalysts. The TOF activity for the different catalysts is: RhANd10 ~ RhANd1> and RhA, at 700 °C (Table 4). The catalysts with the largest crystallite size ≥2.1 nm, RhANd1 and RhANd10 catalysts are more active than the very small Rh particles ~1.0 nm, RhA catalyst (Table 4). The very small rhodium crystallites of the high dispersed RhA sample shows low activity per site. Some authors studying the Pd addition to Rh showed a decrease in TOF which was explained by a reduction of Rh sites for the hydrogenation of aromatic rings [40]. This lesser ability of very small Rh crystallites was consistent with mononuclear inorganic clusters of Rh in homogeneous catalysis. The electronic properties of such very small particles are quite different of the bulk metal [41]. On the other hand, larger Rh particles could present active sites for the reaction, where the methane could adsorb showing higher activity. In the present catalysts could be considered that RhANd1 and RhANd10 with higher size of crystallite would be more accessible sites. When the temperature increases at 750 °C all catalysts present a decrease in activity (Fig. 7), this decrease in conversion could be due to a sintering of the particle size or a deposit of carbon on the surface of the catalyst.

The highest hydrogen production was observed at 700 °C on RhANd10 catalyst (largest particle size, 3.3 nm and highest neodymium concentration). This catalyst presents a hydrogen selectivity of 100%. The catalyst with sizes of particle ≤2.1 nm showed lower selectivities to hydrogen of 89 and 65% on RhA and RhANd1 respectively. One of the important factors that affect the performance of the metal is related to their electronic structure. This is associated to the structure of the

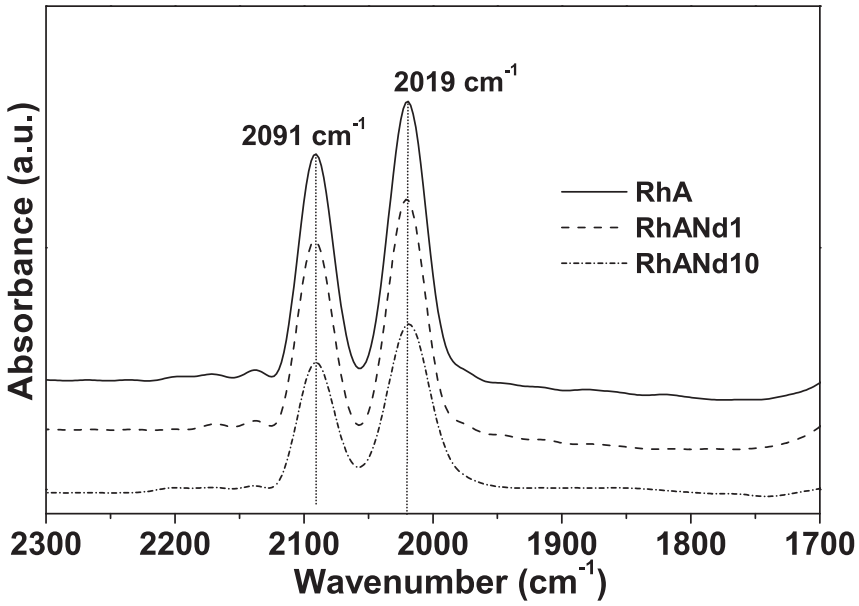

Fig. 6 – FTIR spectra of CO adsorbed on RhA and RhANdX catalysts.

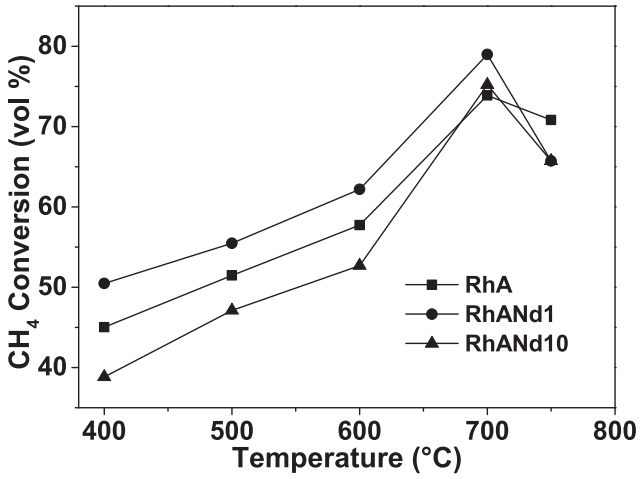

Fig. 7 – Conversion of methane decomposition as a function of temperature for Rh catalysts.

Table 3 – Conversion, selectivity and TOF for the methane dehydrogenation on RhANdX catalysts at 400 °C.

Catalyst	CH_4 conversion (%)	H_2 selectivity (%)	TOF h^{-1}
RhA	45	22	5.5
RhANd1	50	17	14.0
RhANd10	39	26	14.0

particle size [41]. The small metal particles present higher sites of low coordination as corners, edges which are more electro-deficient. Another important parameter to consider is the degree of interaction between metal and support. The charge transfer between the metal-support interfaces can change the d-band density of states and therefore lead to different catalytic properties [37]. The H_2-TPR and XPS studies showed that it exists a high interaction between Rh and γ-Al_2O_3–Nd_2O_3 support which depends of the amount of neodymium surface enrichment on the catalyst. A γ-Al_2O_3 surface rich on neodymium oxide (10 wt%) leads to a strong surface interaction between Rh–Nd_2O_y–γ-Al_2O_3 support [28]. The low content of Nd (1 wt%) on the alumina produces Rh-support interaction, similar to that showed on γ-Al_2O_3 (Figs. 4 and 5). The difference in the degree of interaction of Rh with the support induces changes in the electronic structure, which affect the activity and selectivity of methane decomposition.

Indeed as it is observed in Table 4, the selectivity pattern on RhANd10 catalyst is different to that observed on RhA and RhANd1 catalysts. The CH_4 adsorbs dissociatively on Rh surface particles producing H_2 and CHx (x = 3–0) species. If the CHx species have high mobility on the metal surface, consequently a recombination with another species could be leading to the formation of higher hydrocarbons [42]. It has been reported that the main specie observed in the decomposition of CH_4 is the C_2 hydrocarbons and it depends of the nature of the support [37]. As it can be seen in Table 4, the products detected, in addition to the hydrogen, in the RhA and RhANd1 catalysts are ethane and ethylene whose selectivities are 3 and 8% for the first one and 12 and 23% respectively for the second one, at 700 °C. Studies on the methane conversion and chemisorptions on metallic surfaces showed that CH_3 is the main dissociated specie and the coupling of CH_3 can produce ethane [42]. Further dehydrogenation to CH_2 and coupling leads to the ethylene formation. These products are favored on the Rh surface, in RhA and RhANd1 catalysts, since the adsorption strength allows the migration of the CHx species over the surface. Fig. 9 a) represent the behavior of RhA and RhANd1 catalysts where the interaction with the support is very similar favoring the migration of the CHx species and forming the ethane and ethylene products. On the other hand, due to on RhANd10 catalysts the species CHx are further

Table 4 – Conversion, selectivity and TOF for the methane dehydrogenation on RhANdX catalysts at 700 and 750 °C.

Catalyst	Temperature (°C)	Conversion (%)	TOF (h^{-1})	Selectivity (%)		
				H_2	C_2H_4	C_2H_6
RhA	700	74	9	89	8	3
	750	71	–	85	8	7
RhANd1	700	79	20	65	23	12
	750	68	–	63	12	25
RhANd10	700	75[a]	26	100	0	0
	750	66	–	100	0	0

Theoretical value of the decomposition of CH_4 = 3.2 mmol of H_2 min^{-1} g_{cat}^{-1}.
[a] Experimental value for the decomposition of CH_4 = 2.5 mmol of H_2 min^{-1} g_{cat}^{-1}, with 75% conversion.

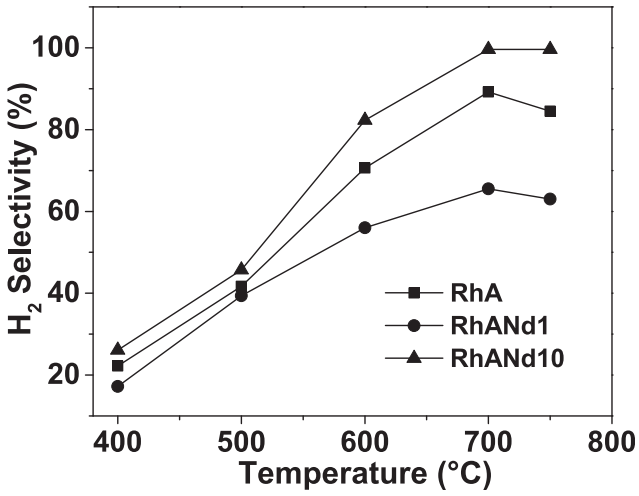

Fig. 8 – Selectivity to hydrogen production as a function of temperature for the methane decomposition on Rh supported on alumina-neodymium catalysts.

adsorbed and are more stable on the Rh surface, the dissociative chemisorption of methane species produces the H_2 evolution, resulted from the association of hydrogen atoms, the only product detected in this catalyst, Fig. 9 b). There were no other products detected due to the strong adsorption of CHx species on the surface.

To determine the stability of the RhANd10 catalyst, the sample, was maintained in time on stream (TOS) for 10 h at 700 °C, as it is showed in Fig. 10, the selectivity remained. As well, with the increase of reaction temperature at 750 °C the selectivity toward hydrogen stayed unchanged at 100%, Fig. 8. The hydrogen production tends to a stable performance as temperature increases. The fact that in RhANd10 catalyst does not decrease the selectivity, even if the carbon is deposited on the Rh surface particles, could be explained by assuming that the carbon deposited can be participating in the reaction acting as an active site [43]. It has been reported that C can dissolve into Rh at elevated temperatures and that part of the dissolved C accumulates at the surface on Rh particles [44]. However, a probable explanation is that the improvement can be due by the release of the H_2 from methane decomposition

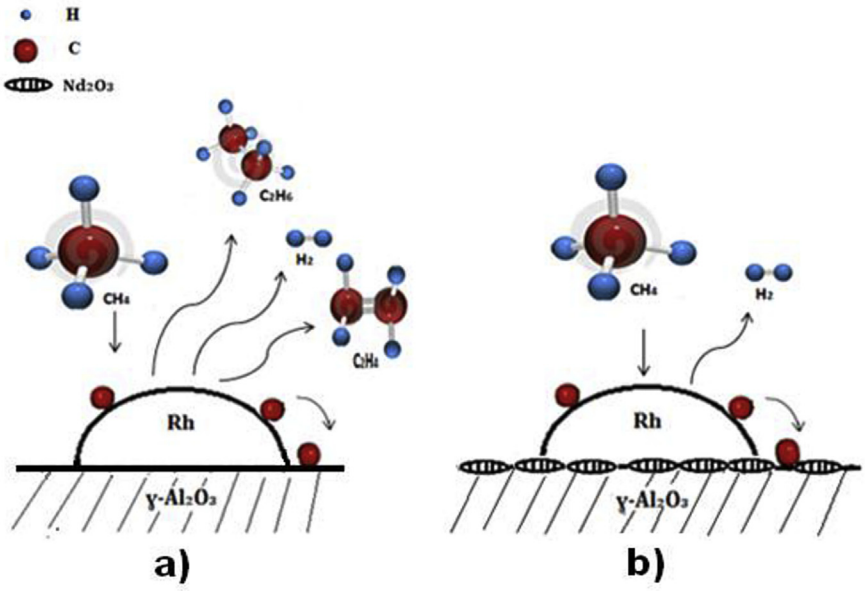

Fig. 9 – Representation of the behavior of methane decomposition on Rh metallic particles for: a) RhA and b) RhANd10 catalysts.

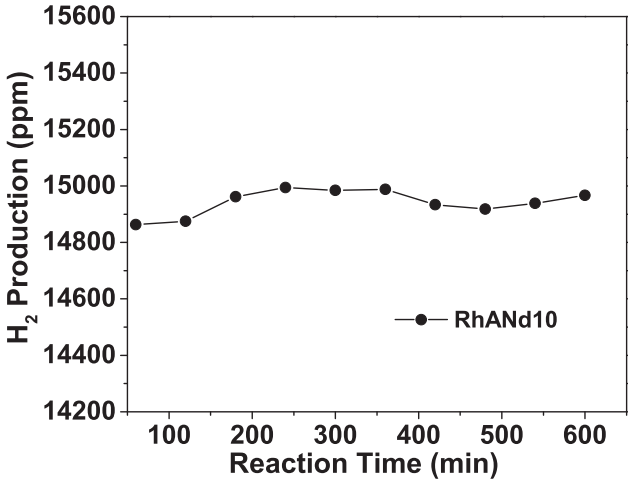

Fig. 10 – Stability test of RhANd10 catalyst for 600 min on time on stream at 700 °C.

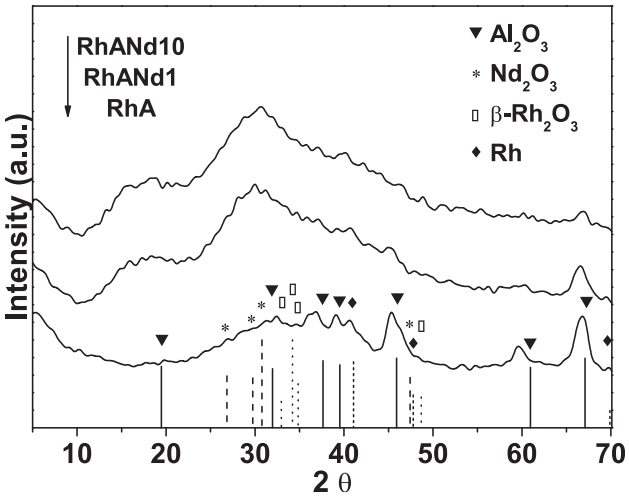

Fig. 11 – X-ray diffractions patterns for all Rh used catalysts.

leading to the reduction of the whole rhodium active sites available for the reaction [45].

In Table 5 is reported the mean Rh crystallite size for the fresh and for the RhANd10-used catalyst and the distribution of crystallite size are showed in Fig. 3 a) and 3 b). The used catalyst is obtained after reaction at the different temperatures: 400, 500, 600, 700 and 750 °C. The fresh catalyst showed a particle size of 3.3 nm and the used catalyst a mean crystallite size of 4.3 nm due to the sintering of Rh particles. However, the activity was not affected. On the contrary RhA and RhANd1 catalysts showed a slight decrease in the selectivity when the temperature increased at 750 °C (Fig. 8), a different surface structure on the Rh particles could be formed with the sintering of the Rh particles and the deposit of dehydrogenated carbonaceous species on the active sites can occurred, inhibiting the dehydrogenation of CH_4.

In the course of the methane decomposition over the Rh surface a deposit of the carbonaceous intermediates is produced. It has been detected various types of carbon formed on the surface of the catalysts according to the reaction temperature: carbidic carbon, amorphous carbon, graphitic carbon [46]. The deposit of carbon on the rhodium could block some active sites and deactivate the catalyst and then modify the selectivity.

The deposited carbon on the RhA, RhANd1 and RhANd10 used catalysts was studied by X-ray diffraction (XRD). The XRD patterns for all the used catalysts are exhibit in Fig. 11. It is observed a similar XRD spectra for the rhodium bare catalyst RhA and the RhA-used catalysts respect to the position of the main peaks characteristic of the γ-alumina (2θ = 67, 45.9 and 37.6°), but showing less intensity in the used sample, which indicate a loss of crystallinity of the Alumina. The peaks in the region 2θ < 40° shown a broad signal caused by the presence of carbon on the used catalyst. It is also perceived a peak, in RhA-used catalyst, at 2θ = 40.069° which correspond to the Rh (111), the detection of this peak is due to the sintering of the Rh metal after reaction, since, it was no detected on the fresh catalyst.

A similar diffraction pattern has been observed for the two used catalysts containing Nd RhANd1 and RhANd10 (Fig. 11). It is clearly observed only one peak typical of the γ-Al_2O_3, placed at 2θ = 67° which intensity is lower due to the crystallinity loss of both samples. The diffraction pattern shows 2 broad and upper peaks caused by the presence of the carbon formed and deposited on the catalyst, which was characterized as amorphous carbon. The very similar pictures showed by the two neodymium promoted Rh catalysts indicate that the presence of neodymium could be the responsible of this behavior acting as a trap of the carbon.

In Fig. 12 is displayed the SEM-EDS analysis of the RhANd10 used-catalyst for mapping and composition exploration. The X-ray maps disclose the elements present in the sample as Al, O, Nd, Rh and C, which correspond to Al_2O_3 and Nd_2O_3, Rh, and C. The Table inset in the Fig. 12, shows the wt% of each element present in the sample of the catalyst. As it can be observed in the mapping of each element, the profiles of Al, O and C present a profile very similar indicating that the carbon present in the catalyst is placed mainly on the surface of the alumina support. In Table 5, is reported the carbon amount on the catalyst determined by SEM-EDS for the RhANd10 used catalyst that is about 18.6 wt%.

The study of HRTEM was carried out with the aim to identify the phases on the catalysts and analyze the type of carbon formed on the surface of the selected RhANd10 sample during the reaction. Fig. 13 shows a high resolution image of a region of the RhANd10 used sample with their respective

Table 5 – Size of crystallite for Rh catalysts: fresh and used in methane decomposition.

Catalyst	d (nm)[a]	d_1 (nm)[b]	Amorphous carbon[c]
	Fresh	Used	(wt%)
RhANd10	3.3 ± 0.7	4.3 ± 1.2	18.61 ± 0.83

[a] d = mean crystallite size by TEM.
[b] d_1 = mean crystallite size by TEM for the catalyst after reaction at different temperatures (400–750 °C).
[c] Amorphous carbon = wt% of C deposited on the surface of the catalyst after reaction, determined by EDS-SEM.

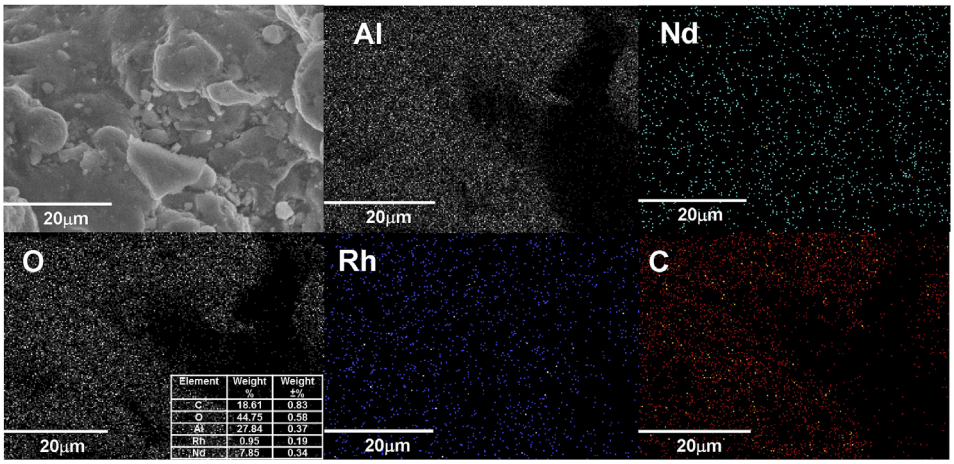

Fig. 12 – SEM and EDS dot mapping analysis for RhANd10 used catalyst.

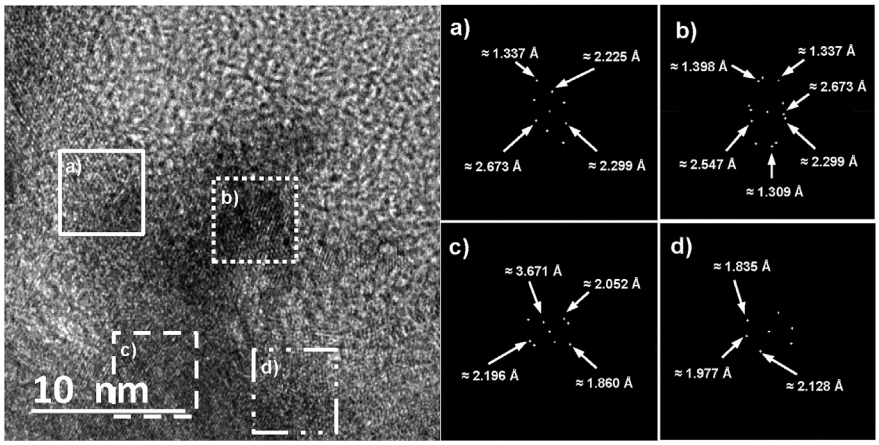

Fig. 13 – HRTEM images of RhANd10 used catalyst with a), b), c) and d) corresponding to FFT of the scanned areas.

Fourier transformed (FFT) of analyzed zones a), b), c) and d). The assignation of the interplanar distances were done by the respective diffraction cards (JPDS) for each of the phase found. The interplanar distance with 1.337, 1.398 and 1.977 Å correspond to the γ-alumina and 2.225 Å to the N_2O_3 (0 1 2) plane. The interplanar distances 2.673, 2.299, 1.309, 3.671 and 1.835 Å correspond to the β-Rh_2O_3 and the 2.196 Å corresponding to the metallic Rh plans (111), the same type of plane for Rh was detected on the RhANd10-used sample by XRD. Finally the interplanar distances of 2.547, 1.86, 2.052 and 2.128 Å correspond to the amorphous carbon.

As it was observed by XRD and High resolution SEM and TEM characterization all carbon produced at around 700 °C is amorphous carbon. In accordance with the XRD and EDS-SEM mapping results can be supposed that carbon is deposited on the support in a great proportion. The XRD present a high modification of the diffraction pattern on the used Rh catalysts containing Nd and in EDS-mapping is observed that the carbon follows the same profiles that the alumina and oxygen, on the same RhANd10 used catalyst, with the deposit of carbon after reaction Figs. 11 and 12. It has been reported that a carbon species diffusion process from the active metal sites, where methane is, towards the alumina support where their interaction with OH and O^{-2} ions take dehydrogenated place [47,48].

This results are more notable in the catalysts containing neodymium in a proportion adequate which favors a high selectivity to hydrogen production, also stabilize the hydrogen production at high temperature and prevent the deactivation in spite of the presence of carbon formed during the reaction. The neodymium oxide deposited on the alumina-Nd support on Rh catalysts could act as a trap for the carbon.

Conclusions

In the present work, it was studied the effect of the Nd_2O_3 (1 and 10 wt%) addition to Rh/γAl_2O_3 for the production of hydrogen in the methane decomposition in the range of temperature of 400–750 °C. Rh/γ-Al_2O_3–Nd_2O_3 the supports and catalysts were prepared by impregnation of the Nd nitrate and $RhCl_3$ as precursors. The catalysts with Rh particle size ≥2.1 nm were more active (TOF) in methane decomposition at

700 °C. The RhANd10 catalyst presented the highest selectivity to hydrogen, 100%. The RhA and RhANd1 catalyst produced 89 and 65% of selectivity of hydrogen respectively and the rest was ethane and ethylene products. The RhANd10 catalyst behavior was explained by the highest interaction of Rh and alumina-Nd_2O_3 support as it was detected by H_2-TPR and XPS studies. The production of ethane and ethylene comes from the mobility of the CHx species on the Rh surface formed during the degradation of methane in RhA and RhANd1 catalysts. The type of carbon produced during the reaction was amorphous carbon which is deposited mainly on the support.

Acknowledgements

We acknowledge to CONACYT for the support provided to the project SEP-CONACYT CB-2013-01-220191 and Marina Caballero Díaz thanks to the CONACYT for the grant awarded No 387137/255851.

REFERENCES

[1] Malaika A, Krzyzynska B, Kozlowwski M. Catalytic decomposition of methane in the presence of in situ obtained ethylene as a method of hydrogen production. Int J Hydrogen Energy 2010;35:7470–5.
[2] Shah N, Panjala D, Huffman JP. Hydrogen production by catalytic decomposition of Methane. Energy Fuels 2001;15:1528–34.
[3] Shah N, Wang Y, Panjala D, Huffman G. Production of hydrogen and carbon nanostructures by Non-oxidative catalytic dehydrogenation of ethane and propane. Energy Fuels 2004;18:727–35.
[4] Wang Y, Shah N, Huffman G. Simultaneous production of hydrogen and carbon nanostructures by decomposition of propane and cyclohexane over alumina supported binary catalysts. Catal Today 2005;99:359–64.
[5] Ahmed S, Ashraf A, Ahmed A, Wasim U, Mostafa A. Effect of Ce and Co addition to Fe/Al_2O_3 for catalytic methane decomposition. Catalysts 2016;6:1–15.
[6] Muradov N. Thermo-catalytic CO_2-free production of hydrogen from hydrocarbon fuels. DOE hydrogen program review. Baltimore, Maryland, USA: The National Renewable Energy Laboratory for the U.S. Department of Energy; 2001. p. 271–96.
[7] Villacampa JI, Royo C, Romeo E, Montoya JA, Del Angel P, Monzón A. Catalytic decomposition of methane over Ni-Al_2O_3 coprecipitated catalysts: reaction and regeneration studies. Appl Catal A 2003;252:363–83.
[8] Takenaka S, Ogihara H, Yamanaka I, Otsuka K. Characterization of silica-regeneration studies. Appl Catal A 2003;252:363–83. Synchrotron Radiat 2001;8:587-589.
[9] Dunker AM, Kumar S, Mulawa PA. Production of hydrogen by thermal and decomposition of methane in a fluidized-bed reactor e effects of catalyst, temperature, residence time. Int J Hydrogen Energy 2006;31:473–84.
[10] Muradov N. Hydrogen via methane decomposition: an application for decarbonization of fossil fuels. Int J Hydrogen Energy 2001;26:1165–75.
[11] Ermakova MA, Ermakov DY. Ni/SiO_2 and Fe/SiO_2 catalysts for production of hydrogen and filamentous carbon via methane decomposition. Catal Today 2002;77:225–35.
[12] Steinberg M, Cheng HC. Modern and prospective technologies for hydrogen production from fossil fuels. Int J Hydrogen Energy 1989;14:797–820.
[13] Makoa M, Coville N, Sokolovskii V. Characterization of Co/Mg/Al_2O_3 high pressure partial oxidation catalysts. Catal Today 1999;49:11–6.
[14] Avdeeva L, Reshetenko T, Ismagilov Z, Likholobov V. Iron-containing catalysts of methane decomposition: accumulation of filamentous carbon. Appl Catal A 2002;228:53–63.
[15] Lee K, Han G, Yoon K, Lee B. Thermocatalytic hydrogen production from the methane in a fluidized bed with activated carbon catalyst. Catal Today 2004;93–95:81–6.
[16] Ibrahim AA, Fakeeha AH, Al Fatesh AS, Abasaeed AE, Khan WU. Methane decomposition over iron catalysts for hydrogen production. Int J Hydrogen Energy 2015;40:7593–600.
[17] ChesnokovVV ChiChkan AS. Production of hydrogen by methane catalytic decomposition over Ni-CuFe/Al_2O_3 catalyst. Int J Hydrogen Energy 2009;34:2979–85.
[18] Muradov N. CO_2-free production of hydrogen by catalytic pyrolysis of hydrogen fuel. Energy Fuels 1998;12:41–8.
[19] Moiliner R, Suelves I, Lázaro MJ, Moreno O. Thermocatalytic decomposition of methane over activated carbons: influence of textural properties and surface chemistry. Int J Hydrogen Energy 2005;30:293–300.
[20] Rostrup-Nielsen JR, Sehested J, Norskov JK. Hydrogen and synthesis gas by steam CO_2 reforming. Adv Catal 2002;47:65–139.
[21] Ferro S. Physicochemical and electrical properties of praseodimium oxides. Int J Electrochem 2011;2011:1–17.
[22] Fakeeha AH, Khan Wl-Fatesh AS, Ibrahim AA, Abasaeed AE. Production of hydrogen from methane over lanthanum supported bimetallic catalysts. Int J Hydrogen Energy 2016;41:8193–8.
[23] Pudukudy Manoj, Yaakob Zahira, Takriff Mohd Sobri. Methane decomposition into COx free hydrogen and multiwalled carbonnanotubes over ceria, zirconia and lanthana supported nickel catalysts prepared via a facile solid state citrate fusion method. Energy Convers Manag 2016;126:302–15.
[24] Al-Fatesh Ahmed Sadeq, Amin Ashraf, Ibrahim Ahmed Aidid, Khan Wasim Ullah, Soliman Mostafa Aly, AL-Otaibi Raja Lafi, et al. Effect of Ce and Co addition to Fe/Al_2O_3 for catalytic methane decomposition. Catalysts 2016;6:40.
[25] Tang L, Yamaguchi D, Burke N, Trimm D, Chiang K. Methane decomposition over ceria modified iron catalysts. Catal Commun 2010;11:1215–9.
[26] López-Vinasco AM, Favier I, Pradey C, Huerta L, Guerrero-Rios I, Teuma E, et al. Unexpected bond activations promoted by palladium nanoparticles. Dalton Trans 2014;43:9038–44.
[27] Rangel-Vázquez I, Del Angel G, Bertin V, Gonzalez F, Vazquez-Zavala A, Arrieta A, Padilla JM, et al. Synthesis and characterization of Sn doped TiO_2 photocatalysts: effect of Sn concentration on the textural properties and on the photocatalytic degradation of 2,4-dichlorophenoxyacetic acid. J Alloys Comp 2015;643:144–9.
[28] Tanabe T, Morikawa A, Hatanaka M, Takahashi N, Nagai Y, Soto A, et al. The interaction between supported Rh- and N_2O_3- enriched surface layer on ZrO_2 for Rh sintering suppression. Catal Today 2012;184:219–26.
[29] Ojeda M, López-Granados M, Rojas S, Terreros P, García–García FJ, Fierro JLG. Manganese-promoted Rh/Al_2O_3 for C_2 oxygenates synthesis from syngas effect of manganese loading. Appl Catal 2004;261:47–55.
[30] Hwang CP, Yeh CT. ZhuQ. Rhodium-oxide pecies formed on progressive oxidation of rhodium clusters dispersed on alumina. Catal Today 1999;51:93–101.

[31] Ferrandon M, Krause T. Role of the oxide support on the performance of Rh catalysts for the autothermal reforming of gasoline and gasoline surrogates to hydrogen. Appl Catal A General 2006;311:135–45.
[32] Burch R, Loader PK, Cruise NA. An investigation of the deactivation of Rh/Alumina catalysts strong oxidizing conditions. Appl Catal A General 1996;147:375–94.
[33] Taniguchi T, Lizuka W, Nagata Y, Uchida T, Samanta H. Magnetic properties of $RRhO_3$ (R=rare earth). J Alloys Compd 2003;350:24–9.
[34] Borg H, Vanden Oetelaar LCA, Niemantsverdriet JW. Preparation of a rhodium catalyst from rhodium trichloride on a flat, conducting alumina support studied with static secondary ion mass spectroscopy and monochromatic ion mass spectrometry and monochromatic X-ray photoelectron spectroscopy. Catal Lett 1993;17:81–95.
[35] Lafaye G, Mihut C, Specel C, Marecot P, Armiridis MD. FTIR studies of CO adsorption on Re-Ge/Al_2O_3 catalysts prepared by surface redox reaction. Langmuir 2004;20:10612–6.
[36] Yates JT, Duncan TM, Vaughan RW. Infrared of chemisorbed CO on Rh. J Chem Phys 1979;70:1219–24.
[37] Ma J, Reng S, Pan D, Li R, Xie K. PVP-Pt nanoclusters supported zeolite catalysts for concerting methane to high hydrocarbon at low temperature. React Funct Polym 2005;62:31–9.
[38] Liang C, Ma Z, Lin H, Ding H, Qiu J, Frandsen W, et al. Template preparation of nanoscale CexFe1-xO2 solid solutions and their catalytic properties for ethanol steam reforming. J Mater Chem 2009;19:1417–24.
[39] Perez-Alonso FJ, López-Granados M, Ojeda M, Terreros P, Rojas S, Herranz T, et al. Chemical structures of coprecipitated Fe-Ce mixed oxides. Chem Mater 2005;17:2329–39.
[40] Del Angel GA, Coq B, Ferrat G, Figueras F. Some catalytic properties of palladium and Rhodium supported catalyst. Surf Sci 1985;156:943–51.
[41] Sheu LL, Knszinger H, Sachtler WMH. Palladium carbonyl clusters entrapped in NaY zeolite cages: ligand dissociation and cluster-wall interactions. Cent Catal Surf Sci 1989;111:8125–31.
[42] Lin YZ, Sun J, Yi J, Lin JD, Chen HB, Liao DW. Energetics of chemisorption and conversion of methane on transition metal surface. J Mol Struct Theochem 2002;587:63–71.
[43] Dong GC, Baarle DWV, Rost MJ, Frenken JWM. Graphene formation on metal surfaces investigated by in-situ scanning tunneling microscopy. New J Phys 2012;14:15.
[44] DeLouise LA, Winogran N. Carbon Monoxide adsorption and desorption on Rh(111). Surf Sci 1984;138:417–31.
[45] Al Fatesh AS, Amin A, Ibrahim AA, Khan WV, Soliman MA, Otaibi RL, et al. Effect of Ce and Co addition to Fe/Al_2O_3 for catalytic methane decomposition. Catalysts 2016;6:40–55.
[46] Otaa A, Kunkesa EL, Krohnerta J, Schmalb M, Behrensa M. Particle size effect in methane activation over supported palladium nanoparticles. Appl Catal A General 2013;452:203–13.
[47] Martins RL, Baldanza MA, Souza MMVM, Schmal M. Methane interaction with silica and alumina supported metal catalysts. Stud Surf Sci 2004;147:643–8.
[48] Ferreira-Aparicio P, Rodríguez-Ramos I, Guerrero Ruíz A. Methane interaction with silica and alumina supported metal catalysts. Appl Catal A General 1997;148:343–56.